

Superconductivity in a van der Waals layered quasicrystal

**Yuki Tokumoto^{1*}, Kotaro Hamano¹, Sunao Nakagawa¹, Yasushi Kamimura¹,
Shintaro Suzuki², Ryuji Tamura^{3,4} & Keiichi Edagawa^{1,4*}**

¹*Institute of Industrial Science, The University of Tokyo, Tokyo 153-8505, Japan*

²*Department of Physical Science, Aoyama Gakuin University, Kanagawa 252-5258,
Japan*

³*Department of Materials Science and Technology, Tokyo University of Science, Tokyo
125-8585, Japan*

⁴*CREST, Japan Science and Technology Agency (JST), Saitama 332-0012, Japan*

* e-mail: tokumoto@iis.u-tokyo.ac.jp; edagawa@iis.u-tokyo.ac.jp

Introductory paragraph

van der Waals (vdW) layered transition-metal chalcogenides are attracting significant attention owing to their fascinating physical properties¹⁻⁵. This group of materials consists of abundant members with various elements, having a variety of different structures. However, all vdW layered materials studied to date have been limited to crystalline materials, and the physical properties of vdW layered quasicrystals have not yet been reported. Here, we report on the discovery of superconductivity in a vdW layered quasicrystal of Ta_{1.6}Te (refs. 6,7). The electrical resistivity, magnetic susceptibility, and specific heat of the Ta_{1.6}Te quasicrystal fabricated by reaction sintering, unambiguously validated the occurrence of bulk superconductivity at a transition temperature of ~1 K. This discovery can pioneer new research on assessing the physical properties of vdW layered quasicrystals as well as two-dimensional quasicrystals; moreover, it paves the way toward new frontiers of superconductivity in thermodynamically stable quasicrystals, which has been the predominant challenge facing condensed matter physics since the discovery of quasicrystals almost four decades ago.

In 1984, Shechtman et al. discovered an exotic solid phase in a rapidly quenched Al–Mn alloy, which exhibited an electron diffraction pattern comprising sharp Bragg spots arranged in ten-fold rotational symmetry⁸. The sharp diffraction spots indicated the existence of a long-range translational order, and the ten-fold symmetric diffraction pattern was incompatible with a periodic order, thus verifying that the phase could not be crystalline. Soon after this discovery, a new classification scheme for solids was proposed, with the aforementioned phase denoted a quasicrystal (QC)^{9–11}. Essentially, QCs have a quasiperiodic long-range translational order that is compatible with crystallographically disallowed rotational symmetries such as five-, ten-, and twelve-fold symmetries. Extensive studies have subsequently revealed that QCs are not exceptional but rather ubiquitous, as they have been formed in several binary and ternary systems. Of the 70 QCs that have been reported to date, approximately 40 have been found to be thermodynamically stable¹².

In 1998, Conrad et al. discovered a unique stable QC phase exhibiting dodecagonal symmetry in the compound of Ta_{1.6}Te (ref. 6). This new QC has several notable features that have not been observed to date. First, this phase is the only reported transition-metal chalcogenide QC. Second, this is the only QC of a vdW layered material; its structure is realized through periodic stacking of two-dimensional dodecagonal (dd)-QCs induced by vdW interactions. The structures of this dd-QC phase and the related crystal approximant (CA) phases have been examined by X-ray diffractometry (XRD), electron diffractometry, and high-resolution transmission electron microscopy^{6,7,13–15}. Moreover, a few layers of the dd-QC phase have recently been isolated using standard exfoliation techniques⁷. However, the number of studies on this phase is still very limited because arc-melting, which is usually used for fabrication of QC alloys, cannot be applied since

the melting temperature of Ta is much higher than the boiling temperature of Te; to the best of our knowledge, experimental studies on elucidating the physical properties of the Ta_{1.6}Te dd-QC phase have not been reported.

Therefore, in this study, the electrical resistivity, magnetic susceptibility, and specific heat of a polygrain single-phase Ta_{1.6}Te dd-QC were measured down to low temperatures. The results categorically confirmed the occurrence of bulk superconductivity in a thermodynamically stable QC for the first time at a transition temperature T_c of ~ 1 K. Superconductivity has never been reported for QC phases, except for a recent example of a metastable icosahedral QC (i-QC) phase of Al–Zn–Mg, which demonstrated bulk superconductivity at $T_c \approx 0.05$ K (ref. 16). Recent theoretical studies have suggested that the quasicrystalline superconductivity exhibits unconventional behavior such as the nonzero sum of the momenta of Cooper pair electrons¹⁷ and intrinsic vortex pinning not by impurities and defects¹⁸. Furthermore, the specific heat and I – V characteristic curves of a normal-metal–superconductor tunnel junction have also been expected to display unusual tendencies¹⁹.

Polygrain single-phase samples of the Ta_{1.6}Te dd-QC were fabricated by reaction sintering, powdered, and then subjected to electron diffractometry and XRD analyses (see Methods section). The electron diffraction pattern of the synthesized sample (Fig. 1a) shows an arrangement of sharp spots with dodecagonal symmetry, which is essentially identical to that previously reported for the Ta_{1.6}Te dd-QC phase⁶. A powder XRD profile of the sample was acquired using Cu K α radiation (Fig. 1b); the Cu K α_2 component was removed numerically, yielding a profile that corresponded to the Cu K α_1 component (wavelength: 1.5405 Å). A comparison of this profile with those of the crystalline phases of TaTe₂ and Ta—the materials used for the reaction sintering (Supplementary Fig. 1)—

revealed no traces of these phases in the acquired profile, indicating the completion of the reaction and the formation of another phase. However, because the powder XRD profile of the Ta_{1.6}Te dd-QC phase has not been previously reported, it was constructed based on that of the CA phase of Ta₉₇Te₆₀, whose structure has previously been determined through single-crystal XRD measurements¹⁴. In general, by introducing phason strain to a QC structure, we can obtain a CA structure. Using this relationship, we can calculate the powder XRD profile of a QC phase from that of its CA phase. The principles and procedures underlying the calculation are detailed in Supplementary Section 1.2. The acquired and constructed profiles were compared (Fig. 1b and the magnified profiles in Fig. 1c). Although the peaks in the acquired profile were not adequately resolved in the 2θ region of 33°–47°, the overall agreement was satisfactory; this indicated that the sample comprised entirely of the Ta_{1.6}Te dd-QC phase. We note that comparing the acquired XRD profile with those of the Ta₂₁Te₁₃ and Ta₉₇Te₆₀ CA phases (Supplementary Fig. 9) showed clear discrepancies. The peak indices shown in Fig. 1c refer to the five basis vectors $\mathbf{a}_i^* = a^* \left(\cos\left(\frac{2\pi(i-1)}{12}\right), \sin\left(\frac{2\pi(i-1)}{12}\right), 0 \right)$ ($i = 1-4$) and $\mathbf{c}^* = (0, 0, c^*)$, with a^* and c^* being 0.6942 Å⁻¹ and 0.6047 Å⁻¹, respectively (Supplementary Table 1). Complete data on the powder XRD profile of the Ta_{1.6}Te dd-QC phase are provided in Supplementary Table 3.

The temperature dependence of the electrical resistivity normalized by the value at $T = 300$ K— $\rho/\rho_{300\text{ K}}$ —was analyzed for three different samples (#1–#3; Fig. 2a); the three samples were prepared in the same way and used for repeatability testing. $\rho_{300\text{ K}}$ was approximately 1.7 mΩ·cm for all the samples. $\rho(T)$ gradually increased with decreasing temperature and abruptly descended to zero at a low temperature, indicating

the emergence of superconductivity. Analysis of the temperature dependence of $\rho/\rho_{300\text{ K}}$ below 2 K (Fig. 2b) indicated that $\rho(T)$ abruptly dropped to zero at a midpoint transition temperature $T_c^{\text{mid}} = 0.98\text{ K}$ for all three samples, where $\rho(T_c^{\text{mid}}) = 0.5 \times \rho(1.1\text{ K})$. Examination of the magnetic field dependence of $\rho/\rho_{300\text{ K}}$ for Sample #1 at different temperatures (Fig. 2c) suggests that the superconducting transitions were suppressed by increasing the magnetic field. Similar results were obtained for Samples #2 and #3. By applying the criterion of 50% of the normal state resistivity to define the upper critical field H_{c2} , the temperature dependence of H_{c2} was explored (Fig. 2d) by plotting $-H_{c2}/[T_c(dH_{c2}/dT)_{T=T_c}]$ against T/T_c (that is, h^* vs. t). According to the Werthamer–Helfand–Hohenberg (WHH) theory²⁰, which considers spin–orbit scattering and spin paramagnetism, H_{c2} in the dirty limit (mean free path $l \ll$ coherence length ξ_0) is expressed as follows, in terms of the digamma function:

$$\ln \frac{1}{t} = \left(\frac{1}{2} + \frac{i\lambda_{\text{SO}}}{4\gamma} \right) \psi \left(\frac{1}{2} + \frac{\bar{h} + \frac{1}{2}\lambda_{\text{SO}} + i\gamma}{2t} \right) + \left(\frac{1}{2} - \frac{i\lambda_{\text{SO}}}{4\gamma} \right) \psi \left(\frac{1}{2} + \frac{\bar{h} + \frac{1}{2}\lambda_{\text{SO}} - i\gamma}{2t} \right) - \psi \left(\frac{1}{2} \right), \quad (1)$$

where ψ is the digamma function, $\gamma \equiv \left[(\alpha\bar{h})^2 - \left(\frac{1}{2}\lambda_{\text{SO}} \right)^2 \right]^{\frac{1}{2}}$, and $\bar{h} = \frac{4}{\pi^2} h^* = \frac{4H_{c2}}{\pi^2(-dH_{c2}/dt)_{t=1}}$, with the parameters λ_{SO} and α representing the effects of the spin–orbit scattering and spin paramagnetism, respectively. The obtained data were adequately fit to equation (1) using $\alpha = \lambda_{\text{SO}} = 0$, indicating that the two effects were negligible. Through this fitting, the value of the zero-temperature upper critical field $H_{c2}(0)$ was deduced to be 32 kOe. The dirty-limit superconductivity was consistent with the large residual resistivity shown in Fig. 2a. A similar H_{c2} tendency has been observed for the Al–Zn–Mg i-QC¹⁶.

The magnetic susceptibility and specific heat were investigated to corroborate the occurrence of the bulk superconductivity. The temperature dependence of the magnetic susceptibility χ was monitored at an external magnetic field of 50 Oe under zero-field cooling (ZFC) and field cooling (FC) conditions (Fig. 3a). In the ZFC curve, a sharp drop occurred at an onset temperature of 0.95 K—a value consistent with the transition temperature corresponding to $\rho(T)$ in Fig. 2b; moreover, a large diamagnetism was observed, indicating the exclusion of the magnetic flux owing to the Meissner effect. The low-temperature data in Fig. 3a suggest the existence of the relationship $4\pi\chi \approx -1$ emu/(Oe·cm³), which corresponds to a superconducting volume fraction of ~100%, thereby providing solid evidence of bulk superconductivity. The XRD data (Figs. 1b and 1c) confirmed that this bulk superconductivity emanated from the dd-QC phase.

The temperature dependence of the specific heat C was probed by plotting C/T against T^2 (Fig. 3b). A jump in the C value was clearly observed at $T \approx 1$ K—a value consistent with the transition temperatures corresponding to $\rho(T)$ (Fig. 2b) and $\chi(T)$ (Fig. 3a). The linear behavior of C/T versus T^2 —that is, the relationship $C/T = \gamma + \beta T^2$ —was observed at T^2 values above ~ 1.4 K²; accordingly, the corresponding γ and β values were estimated as 0.0224 mJ/(g·K²) and 0.00532 mJ/(g·K⁴), respectively. The electronic part of the specific heat C_{el} was determined by subtracting the lattice contribution of the specific heat βT^3 from the measured specific heat, and $C_{\text{el}}/\gamma T$ was subsequently plotted against T (Fig. 3c). Although the jump height ΔC_{el} at T_c could not be precisely evaluated owing to the lower limit of the measurement temperature, the expression $\Delta C_{\text{el}} \gtrsim 1.0 \gamma T_c$ was deemed to apply, which is close to the jump height $\Delta C_{\text{el}} = 1.43 \gamma T_c$ expected from the Bardeen–Cooper–Schrieffer (BCS) theory. This large jump further verified the occurrence of the bulk superconductivity.

Using the aforementioned value of β , the Debye temperature θ_D was deduced to be 132 K. Furthermore, the electron–phonon coupling constant λ_{ep} was obtained using the McMillan equation²¹:

$$T_c = \frac{\theta_D}{1.45} \exp \left\{ - \frac{1.04(1 + \lambda_{ep})}{\lambda_{ep} - \mu^*(1 + 0.62\lambda_{ep})} \right\}, \quad (2)$$

where μ^* denotes the Coulomb pseudopotential parameter, which is typically assumed to be 0.13 for superconductors including transition metals. Using $T_c = 0.98$ K and $\theta_D = 132$ K, λ_{ep} was calculated to be 0.52, indicating a weak-coupling superconductivity. In general, the density of a QC phase is approximately the same as that of its CA phase. Therefore, the density of the Ta_{1.6}Te dd-QC phase can be estimated to be 10.6 g/cm³, calculated for the Ta₉₇Te₆₀ CA phase from its structure data¹⁴. Using this value and the estimated values of γ and λ_{ep} , the density of states (for one of the two spin states) at the Fermi level $D(E_F)$ was estimated as 1.24×10^{47} states/(J · m³) using the expression²¹

$$D(E_F) = \frac{3\gamma}{2\pi^2 k_B^2 (1 + \lambda_{ep})}, \quad (3)$$

where k_B is the Boltzmann constant.

Crystalline Ta–chalcogenide systems including Ta₂Se, TaSe₂, and TaS₂ have been found to exhibit superconductivity at ambient pressure^{22,23}; however, the Ta–Te system has not been reported in this regard. The superconducting parameters of several crystalline Ta–chalcogenide systems^{22,23}, the Ta_{1.6}Te dd-QC, Ta (ref. 24), and Al–Zn–Mg i-QC¹⁶ are summarized in Table 1. For a simple metal system of the Al–Zn–Mg i-QC, $\mu^* = 0.1$ was used²¹ in the calculation of λ_{ep} , while for the others $\mu^* = 0.13$ was used. The λ_{ep} values of Ta and Ta₂Se were fairly high, which may be in an intermediate-coupling range. The other systems exhibited sufficiently small λ_{ep} values appropriate for

weak-coupling superconductors, with the λ_{ep} value of the Al–Zn–Mg i-QC being considerably smaller than those of the others. Furthermore, the materials with higher Ta concentrations tended to have higher $D(E_F)$ values, with the Al–Zn–Mg i-QC exhibiting the smallest value among the specimens.

Superconductivity in a quasiperiodic system has recently been investigated using an attractive Hubbard model on a Penrose lattice—a typical two-dimensional quasicrystalline lattice—using the real-space dynamical mean-field theory¹⁷. Unconventional spatially extended Cooper pairs were observed to form under weak-coupling conditions; the sum of the momenta of the Cooper pair electrons was nonzero, in contrast to the zero total momenta of the Cooper pair in conventional BCS superconductivity. Unlike any other known superconductors in periodic systems, the present finding opens up a new research field to investigate unprecedented unique superconducting states, spatially inhomogeneous on *any* length scale reflecting the self-similarity of the quasiperiodic structure¹¹.

In summary, polygrain single-phase Ta_{1.6}Te dd-QC specimens were fabricated by reaction sintering and then subjected to electrical resistivity, magnetic susceptibility, and specific heat measurements in this study. The results unconditionally validated the occurrence of bulk superconductivity at a T_c of ~ 1 K. This is the first example of superconductivity in thermodynamically stable QCs. The temperature dependence of the upper critical field H_{c2} was consistent with the WHH theory in the dirty limit. The extrapolation of H_{c2} to $T = 0$ yielded a value of 32 kOe. These findings are anticipated to motivate further investigations on the physical properties of vdW layered quasicrystals as well as two-dimensional quasicrystals, including unprecedented unique superconductivity theoretically expected for QCs.

References

1. Deguchi, K., Takano, Y. & Mizuguchi, Y. Physics and chemistry of layered Chalcogenide superconductors. *Sci. Technol. Adv. Mater.* **13**, 054303 (2012).
2. Wang, P., Yang, Y., Pan, E., Liu, F., Ajayan, P. M., Zhou, J. & Liu Z. Emerging phases of layered metal chalcogenides. *Small* **18**, 2105215 (2022).
3. Duong, D. L., Yun, S. J. & Lee, Y. H. Van der Waals Layered materials: opportunities and challenges. *ACS Nano* **11**, 11803-11830 (2017).
4. Tan, C., Cao, X., Wu, X.-J., He, Q., Yang, J., Zhang, X., Chen, J., Zhao, W., Han, S., Nam, G.-H., Sindoro, M. & Zhang, H. Recent advances in ultrathin two-dimensional nanomaterials. *Chem. Rev.* **117**, 6225-6331 (2017).
5. Yi, Y., Chen, Z., Yu, X.-F., Zhou, Z.-K. & Li, J. Recent advances in quantum effects of 2D materials. *Adv. Quantum Technol.* **2**, 1800111 (2019).
6. Conrad, M., Krumeich, F. & Harbrecht, B. A dodecagonal quasicrystalline chalcogenide. *Angew. Chem. Int. Ed.* **37**, 1383-1386 (1998).
7. Cain, J. D, Azizi, A., Conrad, M. & Zettl, A. Layer-dependent topological phase in a two-dimensional quasicrystal and approximant. *PNAS* **117**, 26135-26140 (2020).
8. Shechtman, D., Blech, I., Gratias, K. & Cahn, J. W. Metallic phase with long-range orientational order and no translational symmetry. *Phys. Rev. Lett.* **53**, 1951-1953 (1984).
9. Levine, D. & Steinhardt, P. J. Quasicrystals: A New Class of Ordered Structures. *Phys. Rev. Lett.* **53**, 2477-2480 (1984).
10. Levine, D. & Steinhardt, P. J. Quasicrystals, I: Definition and Structure. *Phys. Rev. B* **34**, 596-616 (1986).
11. Socolar, J. E. S. & Steinhardt, P. J. Quasicrystals II: Unit-cell configurations. *Phys.*

- Rev. B* **34**, 617-647 (1986).
12. Tsai, A. P. Discovery of stable icosahedral quasicrystals: progress in understanding Structure and Properties. *Chem. Soc. Rev.* **42**, 5352-5365 (2013).
 13. Conrad, M., Krumeich, F., Reich, C. & Harbrecht, B. Hexagonal approximants of a dodecagonal tantalum telluride – the crystal structure of Ta₂₁Te₁₃. *Mater. Sci. Eng. A* **294-296**, 37-40 (2000).
 14. Conrad, M. & Harbrecht, B. Ta₉₇Te₆₀: a crystalline approximant of a tantalum telluride quasicrystal with twelvefold rotational symmetry. *Chem. Eur. J.* **8**, 3093-3102 (2002).
 15. Krumeich, F., Conrad, M., Nissen, H.-U. & Harbrecht, B. The mesoscopic structure of disordered dodecagonal tantalum telluride: a high-resolution transmission electron microscopy study. *Phil. Mag. Lett.* **78**, 357-367 (1998).
 16. Kamiya, K., Takeuchi, T., Kabeya, N., Wada, N., Ishimasa, T., Ochiai, A., Deguchi, K., Imura, K. & Sato, N. K. Discovery of superconductivity in quasicrystal. *Nat. Comm.* **9**, 154 (2018).
 17. Sakai, S., Takemori, N., Koga, A. & Arita, R. Superconductivity on a quasiperiodic lattice: extended-to-localized crossover of Cooper pairs. *Phys. Rev. B* **95**, 024509 (2017).
 18. Nagai, Y. Intrinsic vortex pinning in superconducting quasicrystals. *Phys. Rev.* **B106**, 064506 (2022).
 19. Takemori, N., Arita, R. & Sakai, S. Physical properties of weak-coupling quasiperiodic superconductors. *Phys. Rev. B* **102**, 115108 (2020).
 20. Werthamer, N.R., Helfand, K. & Hohenberg, P. C., Temperature and purity dependence of the superconducting critical field, H_{c2} . III. Electron spin and spin-orbit

- effects. *Phys. Rev.* **147**, 295-302 (1966).
21. McMillan, W. L., Transition temperature of strong-coupled superconductors. *Phys. Rev.* **167**, 331-334 (1968).
 22. Gui, X., Górnicka, K., Chen, Q., Zhou, H., Klimczuk, T. & Xie, W., Superconductivity in metal-rich chalcogenide Ta₂Se. *Inorg. Chem.* **59**, 5798-5802 (2020).
 23. Harper, J. M. E., Geballe, T. H., & DiSalvo, F. J., Thermal properties of layered transition-metal dichalcogenides at charge-density-wave transitions. *Phys. Rev. B* **15**, 2943-2951 (1977).
 24. Worley, R. D., Zemansky, M. W., & Boorse, H. A., Heat Capacities of vanadium and tantalum in the normal and superconducting phases. *Phys. Rev.* **99**, 447-458 (1955).

Methods

Sample synthesis

Ta_{1.6}Te samples were synthesized by reaction sintering. TaTe₂ and Ta were used as the starting materials at a ratio of 1:3. TaTe₂ was prepared in advance from a 1:2 elemental powder mixture of Ta (Rare Metallic; ~325 mesh, 99.9%) and Te (Rare Metallic; ~100 mesh, 99.99%). The mixture was pressed into a pellet of diameter 10 mm and inserted into a quartz tube, which was subsequently evacuated to $5-6 \times 10^{-4}$ Pa, sealed, and then subjected to two-step annealing (773 K for 24 h, followed by 1,273 K for 24 h). Subsequently, the mixture of the TaTe₂ powder, Ta powder, and a shot (30 – 40 mg) of iodine (FUJIFILM Wako Pure Chemical; 99.9%; used to promote the reaction) was pressed into a 5-mm-thick pellet of diameter 10 mm. The pellet was sealed in an evacuated ($5-6 \times 10^{-4}$ Pa) quartz tube and then sintered at 1,273 K for six days.

Sample characterization

The structures of the sintered samples were examined by powder XRD and electron diffraction. Powder XRD profiles were obtained using a Rigaku diffractometer (RINT-2500V) with Cu $K\alpha$ radiation at 40 kV and 200 mA, a divergence slit open-angle of 0.5° , scattering slit open-angle of 0.5° , receiving slit width of 0.15 mm, rate of $0.5^\circ/\text{min}$, and step of 0.01° . Electron diffraction patterns were obtained using a TEM (JEM-2010F, JEOL) operated at an acceleration voltage of 200 kV.

Physical property measurements

The electrical resistivity was measured using a physical property measurement system (PPMS; Quantum Design) with a four-probe method and a direct current of 25 – 100 μA .

Samples with cross-sectional areas of 2–3 mm × 2–3 mm and lengths of 5–6 mm were used for the electrical resistivity measurements. The magnetic susceptibility was measured using a magnetic property measurement system (MPMS3; Quantum Design) with a ³He refrigerator. The specific heat was measured using the PPMS with the thermal relaxation method.

Acknowledgements

This study was supported by the JST-CREST program (grant no. JPMJCR22O3; Japan) and JSPS KAKENHI Grant Numbers JP19H05821 and JP23K04355). A part of this work was performed using facilities of the Cryogenic Research Center, the University of Tokyo. A part of this work was supported by “Advanced Research Infrastructure for Materials and Nanotechnology in Japan (ARIM)” of the Ministry of Education, Culture, Sports, Science and Technology (MEXT), Grant Number JPMXP1222UT0053.

Author contributions

K.H., S.N., and Y.T. fabricated the samples and performed powder XRD measurements. Y.K. and K.E. analyzed the powder XRD data and constructed the profile. Y.K., K.H., and Y.T. performed the electron diffraction experiments. Y.T., K.H., and K.E. conducted the electrical resistivity and specific heat measurements. S.S., R.T., Y.T., and K.H. conducted the magnetic susceptibility experiments. K.E. designed and supervised the whole project. Y.T. and K.E. cowrote the manuscript. All the authors have discussed the results and contributed to the manuscript.

Table 1 | Superconducting characteristics of the $\text{Ta}_{1.6}\text{Te}$ dodecagonal quasicrystal (dd-QC), other Ta–chalcogenide systems, Ta, and the Al–Zn–Mg i-QC. T_c and θ_D were sourced from the literature. λ_{ep} was calculated from T_c and θ_D using equation (2), where μ^* values of 0.1 and 0.13 were used for the Al–Zn–Mn i-QC and the other systems, respectively. $D(E_F)$ was calculated from λ_{ep} and reported γ using equation (3).

	T_c (K)	θ_D (K)	λ_{ep}	$D(E_F)$ (10^{47} states/J \cdot m ³)	Reference
$\text{Ta}_{1.6}\text{Te}$ dd-QC	0.98	132	0.52	1.24	Present study
Ta_2Se	3.8	271	0.61	1.82	[22]
TaSe_2	0.15	202	0.37	0.685	[23]
TaS_2	0.8	236	0.45	1.19	[23]
Ta	4.4	231	0.67	2.39	[24]
Al-Zn-Mg i-QC	0.05	317	0.27	0.453	[16]

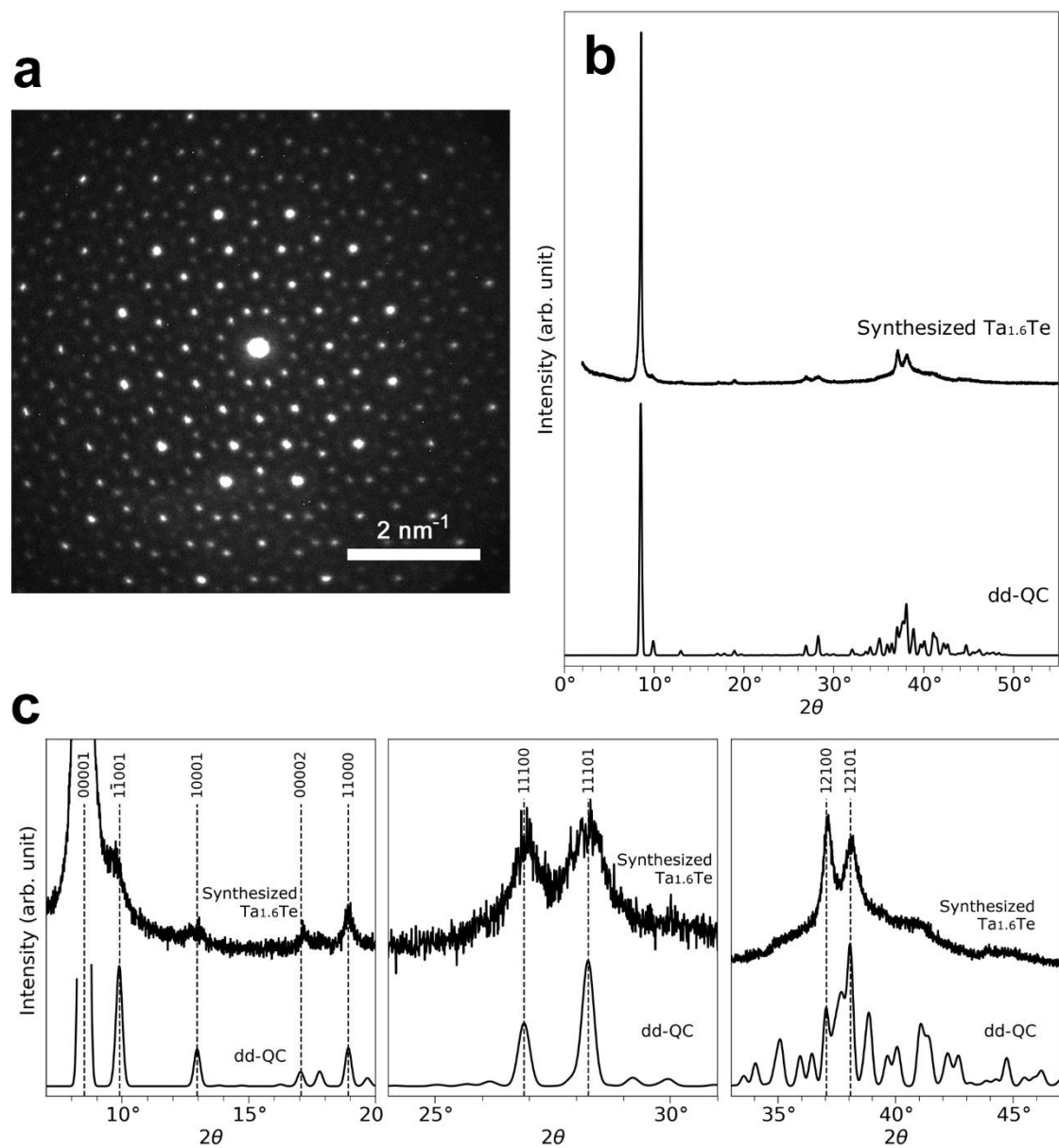


Fig. 1 | Electron and X-ray diffraction data. **a**, Electron diffraction pattern of the synthesized Ta_{1.6}Te. **b**, Experimentally obtained powder XRD profile of the synthesized Ta_{1.6}Te and the calculated profile for the dd-QC phase. **c**, Magnified version of the data shown in **b**. The principles and procedures underlying the calculations are detailed in Supplementary Section 1.2.

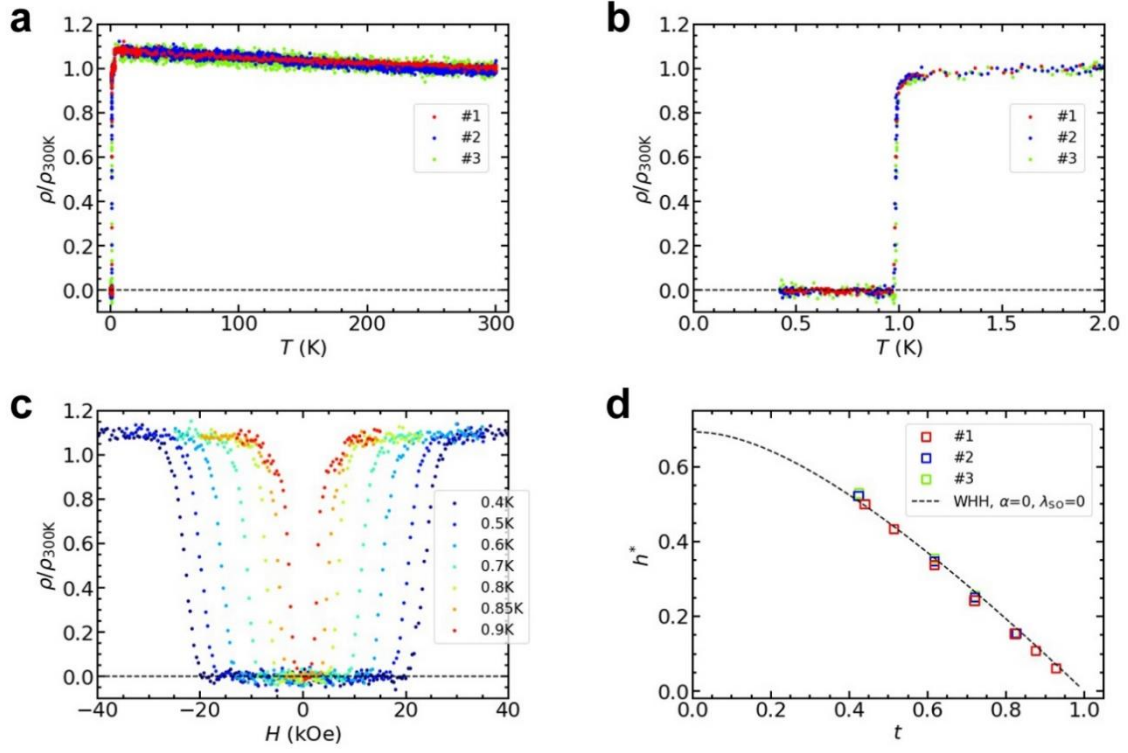


Fig. 2 | Electrical resistivity measurements. **a**, Temperature dependence of the electrical resistivity normalized by the value at $T = 300$ K— $\rho/\rho_{300\text{ K}}$ —for Samples #1–#3. **b**, Temperature dependence of $\rho/\rho_{300\text{ K}}$ for Samples #1–#3 magnified at temperatures below 2 K. **c**, Magnetic field dependence of $\rho/\rho_{300\text{ K}}$ for Sample #1 at different temperatures. **d**, Temperature dependence of the upper critical field H_{c2} analyzed by plotting $h^* = -H_{c2}/[T_c(dH_{c2}/dT)_{T=T_c}]$ against $t = T/T_c$. Open squares represent the experimentally obtained data for Samples #1–#3, and the dashed curve represents the Werthamer–Helfand–Hohenberg (WHH) fit with $\alpha = 0$ and $\lambda_{S0} = 0$.

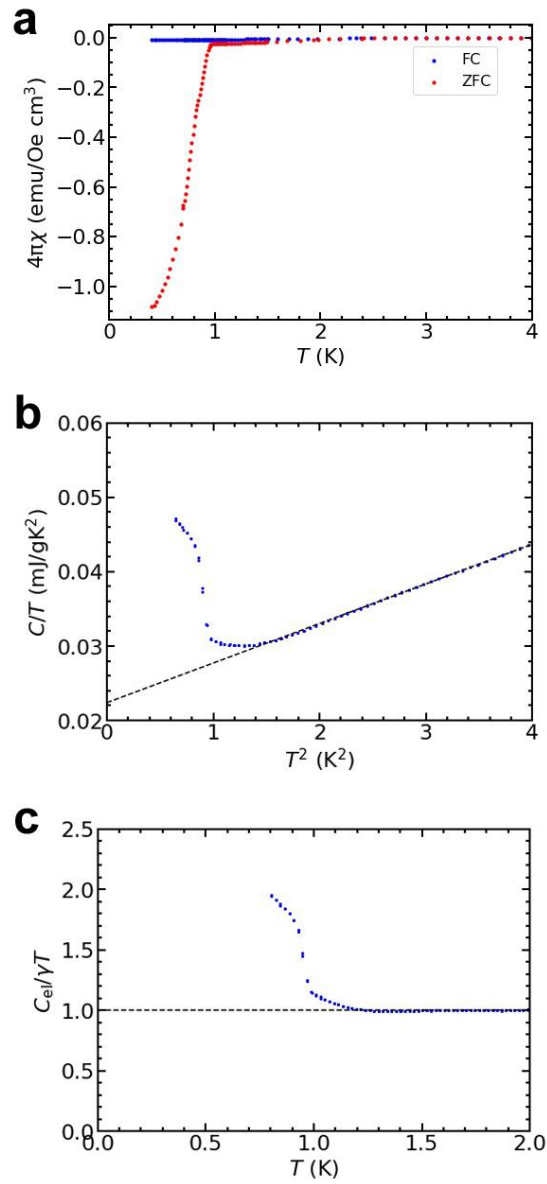


Fig. 3 | Magnetic susceptibility and specific heat measurements. Temperature dependence of **a**, the magnetic susceptibility χ ; **b**, the specific heat C , analyzed by plotting C/T against T^2 ; and **c**, the ratio between the electronic component of the specific heat C_{el} and γT .

Supplementary information

Superconductivity in a van der Waals layered quasicrystal

**Yuki Tokumoto^{1*}, Kotaro Hamano¹, Sunao Nakagawa¹, Yasushi Kamimura¹,
Shintaro Suzuki², Ryuji Tamura^{3,4} & Keiichi Edagawa^{1,4*}**

¹Institute of Industrial Science, The University of Tokyo, Tokyo 153-8505, Japan

*²Department of Physical Science, Aoyama Gakuin University, Kanagawa 252-5258,
Japan*

*³Department of Materials Science and Technology, Tokyo University of Science, Tokyo
125-8585, Japan*

⁴CREST, Japan Science and Technology Agency (JST), Saitama 332-0012, Japan

*e-mail: tokumoto@iis.u-tokyo.ac.jp; edagawa@iis.u-tokyo.ac.jp

Supplementary Discussion 1. Analyses of the powder X-ray diffractometry profiles

1.1. XRD peak indexing

The experimentally acquired X-ray diffractometry (XRD) profile (Cu $K\alpha_1$; $\lambda = 1.5405 \text{ \AA}$) was compared with those of the crystalline phases of the TaTe₂ and Ta materials employed in the reaction sintering (Supplementary Fig. 1). No traces of these phases were observed in the collected profile, indicating the completion of the reaction and formation of another phase.

An attempt was made to index the diffraction peaks in the acquired profile for the dodecagonal quasicrystal (dd-QC). The electron diffraction pattern obtained from the sample revealed dodecagonal symmetry (Supplementary Fig. 2a). All the spots in the pattern were indexed using the four basis vectors \mathbf{a}_i^* ($i = 1-4$) shown in the figure, with $a^* = |\mathbf{a}_i^*| \approx 0.69 \text{ \AA}^{-1}$. The dd-QC phase has been reported to exhibit the periodic stacking of a two-dimensional (2D) quasicrystalline layer with a period of $c \approx 10.4 \text{ \AA}$ (ref. 1). This yields $c^* = |\mathbf{c}^*| = \frac{2\pi}{c} \approx 0.604 \text{ \AA}^{-1}$, where the basis vector \mathbf{c}^* is perpendicular to \mathbf{a}_i^* . Using the five basis vectors \mathbf{a}_i^* ($i = 1-4$) and \mathbf{c}^* , the peaks in the acquired XRD profile were successfully indexed, as shown in Supplementary Fig. 2b and Supplementary Table 1, with the values of a^* and c^* refined to 0.6942 and 0.6047 \AA^{-1} , respectively.

1.2. Construction of the XRD profiles

In this subsection, the calculations performed to construct the profile of the dd-QC phase using one of its crystal approximant (CA) phases are detailed, and a comparison between the calculated and acquired profiles is presented.

1.2.1. CA phases

To date, the structures of two Ta–Te CA phases with compositions Ta₂₁Te₁₃ and Ta₉₇Te₆₀ have been determined using single-crystal XRD measurements^{2,3}. The projections of their structures onto the c -plane (Supplementary Figs. 3a and b) show atomic clusters with dodecagonal symmetry that are arranged periodically. Between the CA phases Ta₂₁Te₁₃ and Ta₉₇Te₆₀, the latter was selected to calculate the dd-QC phase profile. This is an orthorhombic (pseudo-tetragonal) crystal with lattice parameters $a = 27.672$, $b = 27.672$, and $c = 20.613 \text{ \AA}$, with the unit cell in the ab -plane indicated by the blue square in Supplementary Fig. 3b. The basic structure of this phase is a tetragonal crystal with lattice parameters $a = 19.567$ and $c = 10.307 \text{ \AA}$, with the unit cell in the ab -plane indicated by the red square in Supplementary Fig. 3b. A weak superlattice order is introduced into the basic structure of the Ta₉₇Te₆₀ phase. The XRD profiles calculated using VESTA software⁴ from the determined structures of the two CA phases^{2,3} were compared with the acquired profile (Supplementary Fig. 4). The overall features of the collected profile resembled those calculated for the CA phases, highlighting the similarity between the dd-QC and CA phase structures. A more detailed comparison is presented in Supplementary Fig. 9.

1.2.2. Principles underlying the calculation

In general, by introducing phason strain to a QC structure, we can obtain a series of periodic structures, corresponding to CA structures to the QC one. Supplementary Fig. 5a shows a typical one-dimensional (1D) quasiperiodic structure, called the Fibonacci lattice,

which is expressed as a 1D section of a 2D periodic structure. Here, E_{\parallel} is the physical space, and E_{\perp} is the complementary space perpendicular to E_{\parallel} . Furthermore, a line segment on the 2D square lattice spanned by \mathbf{A}_1 and \mathbf{A}_2 exhibits a periodic arrangement, and a 1D point sequence is formed on E_{\parallel} as a set of line segment intersections with E_{\perp} . The slope of E_{\parallel} with respect to the 2D lattice is irrational ($\tau = (1 + \sqrt{5})/2$ in this case), which leads to the point sequence on E_{\parallel} being quasiperiodic instead of periodic.

A phason-strained Fibonacci lattice is shown in Supplementary Fig. 5b. A phason strain can be imposed onto the Fibonacci lattice by applying shear strain to the 2D structure, as indicated by the arrows on the left and right sides of Supplementary Fig. 5a. Upon introducing a shear strain, the vector $\mathbf{t} = \mathbf{A}_1 + 2\mathbf{A}_2$ shown in Supplementary Fig. 5a descends toward E_{\parallel} , as shown in Supplementary Fig. 5b. The structure resting atop E_{\parallel} in Supplementary Fig. 5b exhibits periodicity with a period corresponding to its length. This periodic structure may be regarded as a 2/1 CA to the Fibonacci lattice, because the irrational slope of τ is replaced with a rational slope of 2/1.

The Fourier transform of the Fibonacci lattice can be calculated, as shown schematically in Supplementary Fig. 5c, where E_{\parallel}^* and E_{\perp}^* represent the physical reciprocal space and its complementary space, respectively. First, the Fourier transform of the 2D periodic structure shown in Supplementary Fig. 5a was calculated; this comprised δ -functions at the 2D reciprocal lattice points ($\mathbf{G} = \mathbf{G}_{\parallel} + \mathbf{G}_{\perp}$; $\mathbf{G}_{\parallel} \in E_{\parallel}^*$, $\mathbf{G}_{\perp} \in E_{\perp}^*$) spanned by the basis vectors \mathbf{A}_1^* and \mathbf{A}_2^* shown in Supplementary Fig. 5c. Their intensities were determined through the Fourier transform of the line segment, which was in the form $f(\mathbf{G}_{\perp}) = a \sin(b|\mathbf{G}_{\perp}|)/(b|\mathbf{G}_{\perp}|)$ (a, b : constants) and independent of \mathbf{G}_{\parallel} . This indicates that the reciprocal lattice points with a large $|\mathbf{G}_{\perp}|$ always exhibited small intensities. The Fourier transform $F(\mathbf{q})$ of the Fibonacci lattice could be expressed as the projection of the δ -functions at the 2D reciprocal lattice points onto E_{\parallel}^* , as shown at the bottom of Supplementary Fig. 5c, that is:

$$F(\mathbf{q}) = \sum_{\mathbf{G}} \delta(\mathbf{q} - \mathbf{G}_{\parallel}) \cdot f(\mathbf{G}_{\perp}). \quad (\text{S1})$$

Here, $\mathbf{G}_{\parallel} = h_1 \mathbf{a}_1^* + h_2 \mathbf{a}_2^*$ ($h_1, h_2 \in \text{integers}$), where \mathbf{a}_1^* and \mathbf{a}_2^* are the projections of \mathbf{A}_1^* and \mathbf{A}_2^* onto E_{\parallel}^* , respectively. Because $|f(\mathbf{G}_{\perp})|$ is always small for a large $|\mathbf{G}_{\perp}|$, a threshold value $G_{\perp}^0 (> 0)$ could be used for $|\mathbf{G}_{\perp}|$, and the summation in equation (S1) for \mathbf{G} could be limited to $|\mathbf{G}_{\perp}| < G_{\perp}^0$, that is:

$$F(\mathbf{q}) = \sum_{\mathbf{G} \text{ with } |\mathbf{G}_{\perp}| < G_{\perp}^0} \delta(\mathbf{q} - (h_1 \mathbf{a}_1^* + h_2 \mathbf{a}_2^*)) \cdot f(\mathbf{G}_{\perp}). \quad (\text{S2})$$

The Fourier transform of the 2/1 CA was performed based on the fundamental Fourier transformation attributes, as shown in Supplementary Fig. 5d. This corresponds to the projection of the Fourier transform of the 2D structure shown in Supplementary Fig. 5b. The 2D Fourier transform shown in Supplementary Fig. 5d was obtained by introducing a shear strain to the 2D Fourier transform shown in Supplementary Fig. 5c, as indicated by the arrows on the top and bottom of the figure, which led to the vector $\mathbf{t}^* = -2\mathbf{A}_1^* + \mathbf{A}_2^*$ descending toward E_{\perp}^* . Finally, the Fourier transform of the 2/1 CA was obtained by projecting the 2D Fourier transform onto E_{\parallel}^* , which comprised δ -functions, as shown at the bottom of Supplementary Fig. 5d. If an appropriate value is adopted for G_{\perp}^0 , no more than one 2D reciprocal lattice point will fall onto E_{\parallel}^* at the same position.

Consequently, the Fourier transform of the 2/1 CA can be expressed in the same form as that of equation (S2), but with a different set of basis vectors.

$$F(\mathbf{q}) = \sum_{\mathbf{G} \text{ with } |\mathbf{G}_\perp| < G_\perp^0} \delta(\mathbf{q} - (h_1 \mathbf{b}_1^* + h_2 \mathbf{b}_2^*)) \cdot f(\mathbf{G}_\perp), \quad (\text{S3})$$

where \mathbf{b}_1^* and \mathbf{b}_2^* are the projections of the basis vectors \mathbf{B}_1^* and \mathbf{B}_2^* , respectively, in the 2D reciprocal lattice shown in Supplementary Fig. 5d. Here, the position of the δ -function, $h_1 \mathbf{b}_1^* + h_2 \mathbf{b}_2^*$, can be reindexed using only one basis vector $\mathbf{d}_1^* = \mathbf{b}_1^*$ as $H_1 \mathbf{d}_1^*$, given the relationship $H_1 = h_1 + 2h_2$. Appropriate selection of G_\perp^0 assures one-to-one correspondence between (h_1, h_2) and H_1 . Consequently, if the diffraction intensity function ($I(\mathbf{q}) \equiv |F(\mathbf{q})|^2$) for the Fibonacci lattice can be determined, that for the 2/1 CA can be obtained simply by shifting each δ -function from $h_1 \mathbf{a}_1^* + h_2 \mathbf{a}_2^*$ to $H_1 \mathbf{d}_1^* = (h_1 + 2h_2) \mathbf{d}_1^*$ without changing the intensity and vice versa. This argument should generally hold true for a QC and its CA. Subsequently, this scheme was applied to the dd-QC phase and one of its CA phases, and the XRD profile of the former was calculated using that of the latter.

1.2.3. Four-dimensional description of a dd-QC and its CAs⁵

For a dd-QC and its CAs, a four-dimensional (4D) space spanned by orthonormal unit vectors \mathbf{e}_i ($i = 1 - 4$) can be considered, with \mathbf{e}_1 and \mathbf{e}_2 spanning the physical space E_{\parallel} (E_{\parallel}^*) and \mathbf{e}_3 and \mathbf{e}_4 encompassing the complementary space E_{\perp} (E_{\perp}^*); these can be compared with those in Supplementary Figs. 5a–d. A 4D dd lattice is spanned by \mathbf{A}_i ($i = 1 - 4$) expressed as:

$$\mathbf{A}_i = \sum_{j=1}^4 M_{ij} \mathbf{e}_j, \quad M = \frac{a_{4D}}{\sqrt{2}} \begin{pmatrix} \sqrt{3}/2 & -1/2 & -\sqrt{3}/2 & -1/2 \\ 1 & 0 & 1 & 0 \\ 0 & 1 & 0 & 1 \\ -1/2 & \sqrt{3}/2 & -1/2 & -\sqrt{3}/2 \end{pmatrix}. \quad (\text{S4})$$

Here, a_{4D} is the lattice constant of the 4D lattice. The lattice reciprocal to this 4D lattice is spanned by \mathbf{A}_i^* ($i = 1 - 4$) expressed as:

$$\mathbf{A}_i^* = \sum_{j=1}^4 {}^t M_{ij}^{-1} \mathbf{e}_j, \quad {}^t M_{ij}^{-1} = \frac{a_{4D}^*}{\sqrt{2}} \begin{pmatrix} 1 & 0 & -1 & 0 \\ \sqrt{3}/2 & 1/2 & \sqrt{3}/2 & -1/2 \\ 1/2 & \sqrt{3}/2 & -1/2 & \sqrt{3}/2 \\ 0 & 1 & 0 & -1 \end{pmatrix}. \quad (\text{S5})$$

Here, the superscript t denotes transposition, and a_{4D}^* ($= 4\pi/(\sqrt{3}a_{4D})$) represents the lattice constant of the 4D reciprocal lattice. Supplementary Fig. 6 shows the projections of \mathbf{A}_i (\mathbf{A}_i^*) ($i = 1 - 4$)— \mathbf{a}_i (\mathbf{a}_i^*) and \mathbf{u}_i (\mathbf{u}_i^*)—onto E_{\parallel} (E_{\parallel}^*) and E_{\perp} (E_{\perp}^*), respectively.

A series of square CAs can be obtained by imposing a phason strain onto the 4D dodecagonal lattice, which causes the following two vectors \mathbf{t}_1 and \mathbf{t}_2 to descend toward E_{\parallel} (see Supplementary Figs. 5a and b):

$$\begin{aligned}\mathbf{t}_1 &= (2p, q, p, 0)_{\mathbf{A}_i}, \\ \mathbf{t}_2 &= (0, p, q, 2p)_{\mathbf{A}_i},\end{aligned}\quad (\text{S6})$$

where p and q are integers, and the subscript \mathbf{A}_i indicates that the vectors are represented with respect to the basis vectors \mathbf{A}_i ($i = 1 - 4$). The vectors \mathbf{t}_1 and \mathbf{t}_2 can be rewritten using equation (S4) with the basis vectors \mathbf{e}_i ($i = 1 - 4$) as:

$$\begin{aligned}\mathbf{t}_1 &= \frac{a_{4D}}{\sqrt{2}}(\sqrt{3}p + q, 0, -\sqrt{3}p + q, 0)\mathbf{e}_i, \\ \mathbf{t}_2 &= \frac{a_{4D}}{\sqrt{2}}(0, \sqrt{3}p + q, 0, -\sqrt{3}p + q)\mathbf{e}_i\end{aligned},\quad (\text{S7})$$

Equation (S7) indicates that (1) the E_{\perp} components of \mathbf{t}_1 and \mathbf{t}_2 approach zero as $q/p \rightarrow \sqrt{3}$; (2) the E_{\parallel} components of \mathbf{t}_1 and \mathbf{t}_2 are oriented along \mathbf{e}_1 and \mathbf{e}_2 , respectively, corresponding to the lattice translational vectors of the square CA structure; and (3) the lattice constant of the square lattice can be expressed as:

$$a = \frac{\sqrt{3}p + q}{\sqrt{2}}a_{4D}. \quad (\text{S8})$$

Point (1) suggests that the closer q/p is to $\sqrt{3}$, the more identical is the CA structure to the QC structure.

The introduction of the phason strain changes the basis vectors of the 4D dodecagonal lattice \mathbf{A}_i ($i = 1 - 4$) to \mathbf{B}_i ($i = 1 - 4$). Correspondingly, the basis vectors of the reciprocal lattice \mathbf{A}_i^* ($i = 1 - 4$) are transformed into \mathbf{B}_i^* ($i = 1 - 4$), similar to the case of the Fibonacci lattice shown in Supplementary Figs. 5a–d. On the other hand, equation (S7) and the relationship $a_{4D}^* = 4\pi/(\sqrt{3}a_{4D})$ indicate that the reciprocal basis vectors of the square lattice of the CA— \mathbf{d}_1^* and \mathbf{d}_2^* —can be expressed with respect to the basis vectors \mathbf{e}_1 and \mathbf{e}_2 as:

$$\begin{aligned}\mathbf{d}_1^* &= \frac{a_{4D}^*}{\sqrt{2}}\left(\frac{1}{p + q/\sqrt{3}}, 0\right), \\ \mathbf{d}_2^* &= \frac{a_{4D}^*}{\sqrt{2}}\left(0, \frac{1}{p + q/\sqrt{3}}\right)\end{aligned},\quad (\text{S9})$$

Based on the relationship between the projections of \mathbf{B}_i^* ($i = 1 - 4$) onto E_{\parallel}^* (that is, \mathbf{b}_i^* ($i = 1 - 4$)) and \mathbf{d}_1^* ($i = 1, 2$), the δ -functions at $h_1\mathbf{a}_1^* + h_2\mathbf{a}_2^* + h_3\mathbf{a}_3^* + h_4\mathbf{a}_4^*$ for the dd-QC are linked to those at $H_1\mathbf{d}_1^* + H_2\mathbf{d}_2^*$ for the CA through the expression:

$$\begin{pmatrix} H_1 \\ H_2 \end{pmatrix} = \begin{pmatrix} 2p & q & p & 0 \\ 0 & p & q & 2p \end{pmatrix} \begin{pmatrix} h_1 \\ h_2 \\ h_3 \\ h_4 \end{pmatrix}. \quad (\text{S10})$$

1.2.4. Parameter determination

a^* was determined to be 0.6942 \AA^{-1} for the investigated dd-QC phase (see Section 1.1). This value should be equal to $\frac{a_{4D}^*}{\sqrt{2}}$ in equation (S5), which leads to $a_{4D}^* = 0.9817 \text{ \AA}^{-1}$. Furthermore, the relationship $a_{4D}^* = 4\pi/(\sqrt{3}a_{4D})$ yields an a_{4D} value of 7.390 \AA . The lattice constant (a) of the basic structure of the $\text{Ta}_{97}\text{Te}_{60}$ CA phase was determined to be 19.567 \AA (Section 1.2.1)³. Notably, for $p = 1$ and $q = 2$, equation (S8) yields $a = 19.50 \text{ \AA}$, which is consistent with the lattice constant of the CA phase. Therefore, the $\text{Ta}_{97}\text{Te}_{60}$ phase

was confirmed to be a square CA phase with $p = 1$ and $q = 2$ (tetragonal in 3D). Considering the superlattice ordering in the ab -plane and along the c -direction in the CA phase, as described in Section 1.2.1, the indices (H_1', H_2', H_3') for the superlattice-ordered structure are related to those (H_1, H_2, H_3) for the basic structure as follows:

$$\begin{pmatrix} H_1' \\ H_2' \\ H_3' \end{pmatrix} = \begin{pmatrix} 1 & -1 & 0 \\ 1 & 1 & 0 \\ 0 & 0 & 2 \end{pmatrix} \begin{pmatrix} H_1 \\ H_2 \\ H_3 \end{pmatrix}. \quad (\text{S11})$$

Using equations (S11) and (S10) with $p = 1$ and $q = 2$, the relationship between the indices (H_1', H_2', H_3') for the superlattice-ordered Ta₉₇Te₆₀ CA phase and those $(h_1, h_2, h_3, h_4, h_5)$ for the dd-QC phase can be obtained.

$$\begin{pmatrix} H_1' \\ H_2' \\ H_3' \end{pmatrix} = \begin{pmatrix} 2 & 1 & -1 & -2 & 0 \\ 2 & 3 & 3 & 2 & 0 \\ 0 & 0 & 0 & 0 & 2 \end{pmatrix} \begin{pmatrix} h_1 \\ h_2 \\ h_3 \\ h_4 \\ h_5 \end{pmatrix} \quad (\text{S12})$$

G_1^0 was assumed to be $2.4 \frac{a_4 D}{\sqrt{2}}$, and the XRD profile of the dd-QC phase was calculated using that of the Ta₉₇Te₆₀ CA phase with equation (S12).

1.2.5. Results

Supplementary Table 2 presents the indices, q -value, the structural factor squared $|F|^2$, scattering angle 2θ , and powder diffraction intensity I calculated for the Ta₉₇Te₆₀ CA phase using VESTA software⁴ with the structural data reported by Harbrecht and Conrad³, where $q = (4\pi \sin \theta)/\lambda$, and $\lambda = 1.5405 \text{ \AA}^{-1}$ (CuK α_1). Supplementary Table 3 summarizes the calculation results of the dd-QC phase. Supplementary Figs. 7a and 7b show the diffraction patterns calculated for the Ta₉₇Te₆₀ CA and dd-QC phases on the planes perpendicular to the c -axis, respectively. Supplementary Fig. 8 shows the collected powder XRD profile of the sample and those calculated for the dd-QC, Ta₉₇Te₆₀ CA, and Ta₂₁Te₁₃ CA phases; Supplementary Figs. 9a–d present the magnified versions of these profiles.

References

1. Conrad, M., Krumeich, F. & Harbrecht, B. A dodecagonal quasicrystalline chalcogenide. *Angew. Chem. Int. Ed.* **37**, 1383-1386 (1998).
2. Conrad, M., Krumeich, F., Reich, C. & Harbrecht, B. Hexagonal approximants of a dodecagonal tantalum telluride – the crystal structure of Ta₂₁Te₁₃. *Mater. Sci. Eng. A* **294-296**, 37-40 (2000).
3. Conrad, M. & Harbrecht, B. Ta₉₇Te₆₀: A Crystalline Approximant of a Tantalum Telluride Quasicrystal with Twelffold Rotational Symmetry. *Chem. Eur. J.* **8**, 3093-3102 (2002).
4. Momma, K. & Izumi, F. VESTA 3 for three-dimensional visualization of crystal, volumetric and morphology data. *J. Appl. Crystallogr.* **44**, 1272–1276 (2011).
5. Yamamoto, A. Crystallography of Quasiperiodic Crystals. *Acta Cryst. A.* **A52**, 509–560 (1996).

Supplementary Table 1 | XRD peak indexing results. q_{exp} and q_{calc} denote the experimental and calculated q -values, respectively. $q = \frac{4\pi \sin \theta}{\lambda}$, and $\lambda = 1.5405 \text{ \AA}$.

q_{exp}	Index	q_{calc}
0.608	00001	0.6047
0.688	1 $\bar{1}$ 001	0.7034
0.912	10001	0.9206
1.220	00002	1.2094
1.340	11000	1.3411
1.901	11100	1.8966
1.991	11101	1.9906
2.596	12100	2.5908
2.665	12101	2.6604

Supplementary Table 2 | Powder XRD data for the Ta₉₇Te₆₀ crystal approximant (CA) phase. Indices, q -value, scattering angle 2θ , and relative intensity I calculated for the Ta₉₇Te₆₀ CA phase using VESTA⁴ software with the structural data reported by Harbrecht and Conrad³. $q = \frac{4\pi \sin \theta}{\lambda}$ and $\lambda = 1.5405 \text{ \AA}$.

$H1^\circ$	$H2^\circ$	$H3^\circ$	q	2θ	I
0	0	2	0.6096	8.57	100.00
1	0	2	0.6505	9.15	11.93
1	1	2	0.6890	9.69	2.36
3	1	0	0.7180	10.10	0.36
2	0	2	0.7602	10.69	0.74
2	1	2	0.7934	11.16	2.05
2	2	2	0.8855	12.46	0.74
3	1	2	0.9419	13.26	1.03
0	0	4	1.2193	17.19	0.49
5	2	0	1.2228	17.24	0.23
1	0	4	1.2402	17.49	0.26
1	1	4	1.2608	17.78	0.27
5	3	0	1.3240	18.68	1.10
6	0	0	1.3624	19.23	0.71
3	1	4	1.4150	19.98	0.25
7	2	2	1.7619	24.95	0.22
8	2	0	1.8724	26.54	2.64
8	2	1	1.8970	26.90	0.95
6	6	0	1.9267	27.32	1.23
8	1	2	1.9295	27.37	0.42
6	6	1	1.9506	27.67	0.48
8	2	2	1.9691	27.94	5.13
7	1	4	2.0160	28.62	0.31
6	6	2	2.0208	28.69	2.57
8	3	2	2.0335	28.87	0.23
7	2	4	2.0540	29.17	0.32
8	2	3	2.0838	29.60	0.59
6	6	3	2.1327	30.31	0.31
6	5	4	2.1521	30.60	0.37
8	1	4	2.1995	31.29	0.24
8	2	4	2.2344	31.80	1.33
5	3	6	2.2578	32.14	0.35
6	6	4	2.2801	32.46	0.54
6	0	6	2.2805	32.47	0.22
8	3	4	2.2913	32.63	0.61
7	5	4	2.3026	32.79	0.21
6	2	6	2.3253	33.13	0.54
8	4	4	2.3688	33.76	0.43
9	1	4	2.3904	34.08	0.81
8	2	5	2.4143	34.43	0.68
9	2	4	2.4226	34.55	1.49

7	1	6	2.4337	34.72	1.95
0	0	8	2.4385	34.79	0.24
10	3	2	2.4477	34.92	0.42
6	4	6	2.4547	35.03	1.98
6	6	5	2.4566	35.06	0.34
1	1	8	2.4596	35.10	0.82
8	5	4	2.4648	35.18	0.27
9	3	4	2.4752	35.33	1.23
7	5	5	2.4775	35.36	0.72
2	0	8	2.4805	35.41	1.07
8	7	2	2.4895	35.54	0.38
2	1	8	2.4908	35.56	0.24
9	5	3	2.5102	35.85	0.22
5	3	7	2.5111	35.86	0.21
7	3	6	2.5170	35.95	2.91
2	2	8	2.5217	36.02	1.41
8	4	5	2.5392	36.27	0.70
10	3	3	2.5408	36.30	0.44
3	1	8	2.5420	36.32	2.87
9	4	4	2.5471	36.39	0.39
11	2	1	2.5568	36.54	0.23
7	7	4	2.5572	36.54	0.81
9	1	5	2.5594	36.57	0.88
8	8	0	2.5689	36.71	3.23
6	2	7	2.5720	36.76	0.30
10	0	4	2.5772	36.84	1.87
8	0	6	2.5777	36.84	1.10
8	7	3	2.5811	36.89	0.57
8	8	1	2.5869	36.98	4.50
10	1	4	2.5872	36.99	0.65
8	1	6	2.5877	36.99	0.20
11	3	0	2.5889	37.01	7.54
4	0	8	2.6022	37.21	2.02
11	3	1	2.6068	37.27	8.44
11	2	2	2.6108	37.33	0.80
10	4	3	2.6109	37.34	0.42
10	2	4	2.6170	37.43	1.82
8	2	6	2.6174	37.43	3.07
3	3	8	2.6219	37.50	1.35
9	5	4	2.6366	37.72	1.67
9	3	5	2.6387	37.75	0.66
8	8	2	2.6402	37.77	6.32
4	2	8	2.6415	37.79	2.40
6	6	6	2.6565	38.01	1.73
11	3	2	2.6597	38.06	13.34
10	3	4	2.6657	38.15	1.48
7	1	7	2.6703	38.22	0.60
11	4	1	2.6751	38.29	0.23

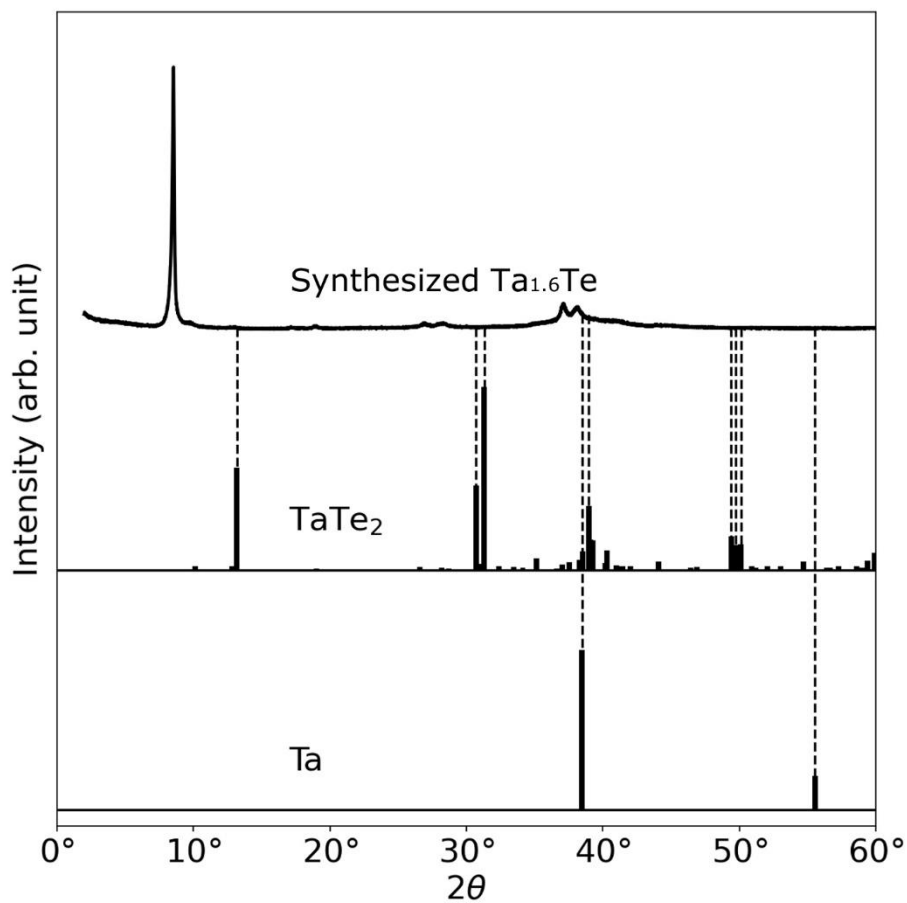
7	5	6	2.6758	38.30	3.47
6	4	7	2.6895	38.50	0.56
5	0	8	2.6899	38.51	0.62
11	2	3	2.6983	38.63	0.70
5	1	8	2.6994	38.65	2.58
8	7	4	2.7042	38.72	1.28
7	7	5	2.7158	38.89	0.50
11	4	2	2.7267	39.06	0.79
8	8	3	2.7268	39.06	3.16
5	2	8	2.7279	39.08	0.30
10	4	4	2.7326	39.15	1.64
8	4	6	2.7330	39.15	3.41
10	0	5	2.7347	39.18	1.15
11	3	3	2.7456	39.34	6.66
7	3	7	2.7464	39.35	0.65
9	1	6	2.7518	39.43	2.67
4	4	8	2.7561	39.50	0.50
10	2	5	2.7721	39.74	0.92
5	3	8	2.7748	39.78	2.87
11	1	4	2.7886	39.98	1.29
9	5	5	2.7907	40.01	0.80
6	0	8	2.7933	40.05	1.10
12	1	2	2.8013	40.17	0.56
10	6	3	2.8014	40.17	0.25
8	0	7	2.8022	40.19	0.23
6	1	8	2.8025	40.19	0.55
11	4	3	2.8106	40.31	0.37
11	2	4	2.8162	40.40	0.78
10	3	5	2.8182	40.43	0.44
9	3	6	2.8258	40.54	2.53
6	2	8	2.8300	40.60	1.90
3	1	9	2.8358	40.69	0.31
8	2	7	2.8388	40.73	0.51
5	4	8	2.8391	40.74	0.40
8	8	4	2.8435	40.80	2.64
8	7	5	2.8546	40.97	0.24
11	3	4	2.8616	41.08	6.11
12	3	2	2.8740	41.26	0.53
6	3	8	2.8751	41.28	0.38
10	4	5	2.8815	41.37	0.90
12	1	3	2.8830	41.40	0.31
7	5	7	2.8927	41.54	0.65
7	7	6	2.8978	41.62	0.73
12	2	3	2.9097	41.80	0.39
10	6	4	2.9152	41.88	0.45
10	0	6	2.9156	41.89	1.95
7	1	8	2.9196	41.95	1.44
11	4	4	2.9240	42.01	0.40

11	1	5	2.9347	42.17	0.34
12	4	2	2.9361	42.19	0.23
6	4	8	2.9372	42.21	1.50
8	4	7	2.9457	42.34	0.39
7	2	8	2.9460	42.34	0.27
10	2	6	2.9507	42.42	1.29
11	2	5	2.9610	42.57	0.23
9	1	7	2.9632	42.60	0.29
9	5	6	2.9681	42.68	0.67
8	8	5	2.9870	42.96	0.66
7	3	8	2.9894	43.00	1.26
11	5	4	3.0023	43.19	0.33
11	3	5	3.0042	43.22	1.54
12	2	4	3.0194	43.45	0.30
9	3	7	3.0320	43.64	0.24
8	0	8	3.0407	43.77	0.32
5	3	9	3.0461	43.86	0.28
0	0	10	3.0482	43.89	0.30
10	4	6	3.0537	43.97	0.28
1	0	10	3.0566	44.02	0.81
1	1	10	3.0650	44.14	0.23
8	2	8	3.0745	44.29	0.62
2	0	10	3.0818	44.40	0.26
2	1	10	3.0902	44.52	0.29
13	1	3	3.0985	44.65	0.24
11	1	6	3.1040	44.73	0.21
6	6	8	3.1078	44.79	0.30
2	2	10	3.1151	44.90	0.79
7	5	8	3.1244	45.04	0.67
3	1	10	3.1316	45.15	2.28
11	3	6	3.1697	45.73	0.25
8	4	8	3.1735	45.79	0.25
4	0	10	3.1806	45.90	0.79
9	1	8	3.1897	46.04	0.20
3	3	10	3.1968	46.15	0.53
14	2	0	3.2111	46.37	0.41
4	2	10	3.2129	46.39	0.24
14	2	1	3.2255	46.59	0.37
5	0	10	3.2527	47.00	0.33
9	3	8	3.2537	47.02	0.27
5	1	10	3.2606	47.12	0.77
14	2	2	3.2685	47.24	0.43
14	4	0	3.3060	47.82	0.41
14	4	1	3.3201	48.04	0.40
5	3	10	3.3233	48.09	0.46
6	0	10	3.3388	48.32	0.35
14	4	2	3.3618	48.68	0.57
14	4	3	3.4302	49.74	0.25

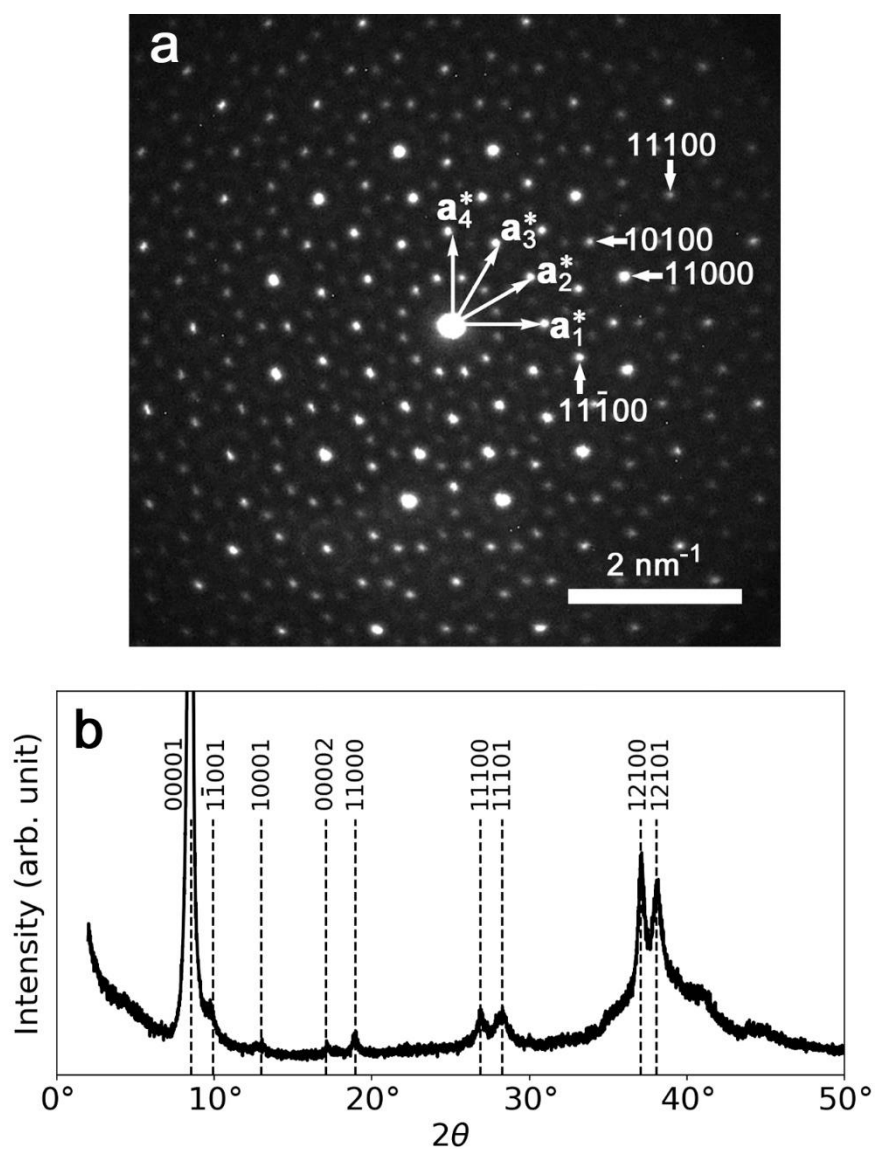
Supplementary Table 3 | Calculated powder XRD data for the dodecagonal quasicrystal (dd-QC) phase. Indices, q -value, scattering angle 2θ , and relative intensity I calculated for the dd-QC phase. $q = \frac{4\pi \sin \theta}{\lambda}$ and $\lambda = 1.5405 \text{ \AA}$.

$h1$	$h2$	$h3$	$h4$	$h5$	q	2θ	I
0	0	0	0	1	0.6047	8.50	100.00
1	0	0	0	0	0.6942	9.76	0.48
1	-1	0	0	1	0.7034	9.89	5.47
1	0	0	0	1	0.9206	12.96	1.77
0	0	0	0	2	1.2094	17.05	0.49
1	-1	0	0	2	1.2617	17.80	0.71
1	1	0	0	0	1.3411	18.93	1.81
1	0	0	0	2	1.3945	19.69	0.36
1	1	1	0	0	1.8966	26.89	3.87
2	0	0	1	2	1.9678	27.92	0.52
1	1	1	0	1	1.9906	28.25	7.70
2	1	-1	0	2	2.0555	29.19	0.48
2	1	0	0	1	2.1082	29.96	0.42
2	1	-1	-1	2	2.2494	32.02	1.87
1	1	0	0	3	2.2560	32.11	0.56
2	0	0	0	3	2.2845	32.53	0.55
2	1	0	0	2	2.3541	33.55	1.44
2	0	0	1	3	2.3876	34.04	3.27
0	0	0	0	4	2.4189	34.50	0.24
1	-1	0	0	4	2.4454	34.89	2.70
2	1	-1	0	3	2.4604	35.11	6.05
1	0	0	0	4	2.5165	35.94	4.28
2	2	-1	0	2	2.5506	36.44	4.67
1	2	1	0	0	2.5908	37.04	10.76
1	0	0	1	4	2.6105	37.33	4.43
2	2	-1	-1	2	2.6188	37.45	2.26
2	1	-1	-1	3	2.6245	37.54	4.81
2	-1	-1	0	4	2.6351	37.70	7.69
3	1	-1	0	2	2.6433	37.82	4.73
1	2	1	0	1	2.6604	38.07	19.60
2	0	-1	0	4	2.7012	38.68	3.08
2	1	0	0	3	2.7148	38.88	9.54
2	2	0	0	1	2.7495	39.40	0.25
1	1	0	0	4	2.7658	39.64	3.97
3	1	0	0	1	2.7729	39.75	0.40
2	0	0	0	4	2.7890	39.99	2.40
3	1	-1	-1	2	2.7968	40.10	3.80
2	2	0	-1	2	2.8592	41.04	7.89
2	0	0	1	4	2.8741	41.26	3.84
2	2	-1	0	3	2.8868	41.45	5.29
3	1	-1	-2	1	2.9195	41.94	0.48
2	1	-1	0	4	2.9348	42.18	3.70
2	2	0	0	2	2.9422	42.29	0.59

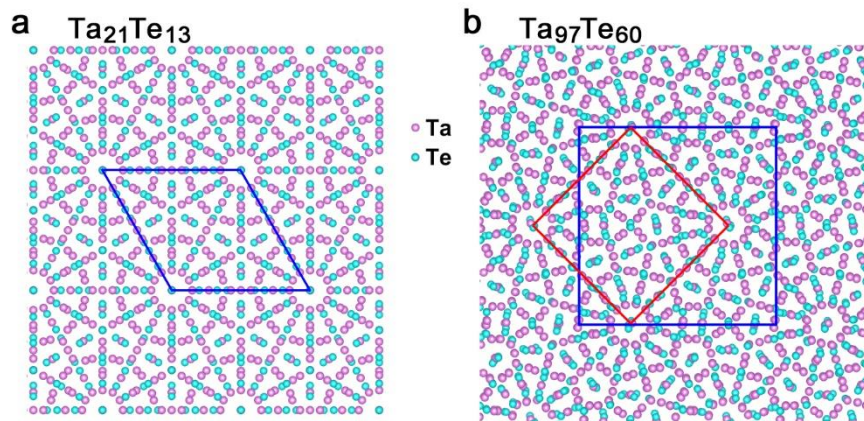
2	2	-1	-1	3	2.9473	42.36	1.20
3	1	0	0	2	2.9641	42.62	1.49
3	1	-1	0	3	2.9691	42.69	2.99
3	2	-1	0	1	3.0009	43.17	0.43
0	0	0	0	5	3.0236	43.52	0.20
1	-1	0	0	5	3.0449	43.84	0.72
3	2	-1	-1	1	3.0591	44.05	0.23
2	1	-1	-1	4	3.0737	44.28	0.92
3	1	-1	-2	2	3.1017	44.70	0.45
1	0	0	0	5	3.1023	44.71	3.07
3	1	-1	-1	3	3.1065	44.77	0.57
2	1	0	0	4	3.1512	45.45	1.12
2	2	0	-1	3	3.1628	45.63	0.25
1	0	0	1	5	3.1790	45.88	0.94
2	-1	-1	0	5	3.1992	46.18	2.07
3	2	-1	-2	0	3.2108	46.36	0.28
2	0	-1	0	5	3.2539	47.02	0.78
3	2	-1	-2	1	3.2672	47.22	0.21
3	2	0	-1	0	3.2849	47.50	0.71
2	2	-1	0	4	3.3005	47.74	0.61
1	1	0	0	5	3.3077	47.85	0.49
3	2	0	-1	1	3.3401	48.35	0.90



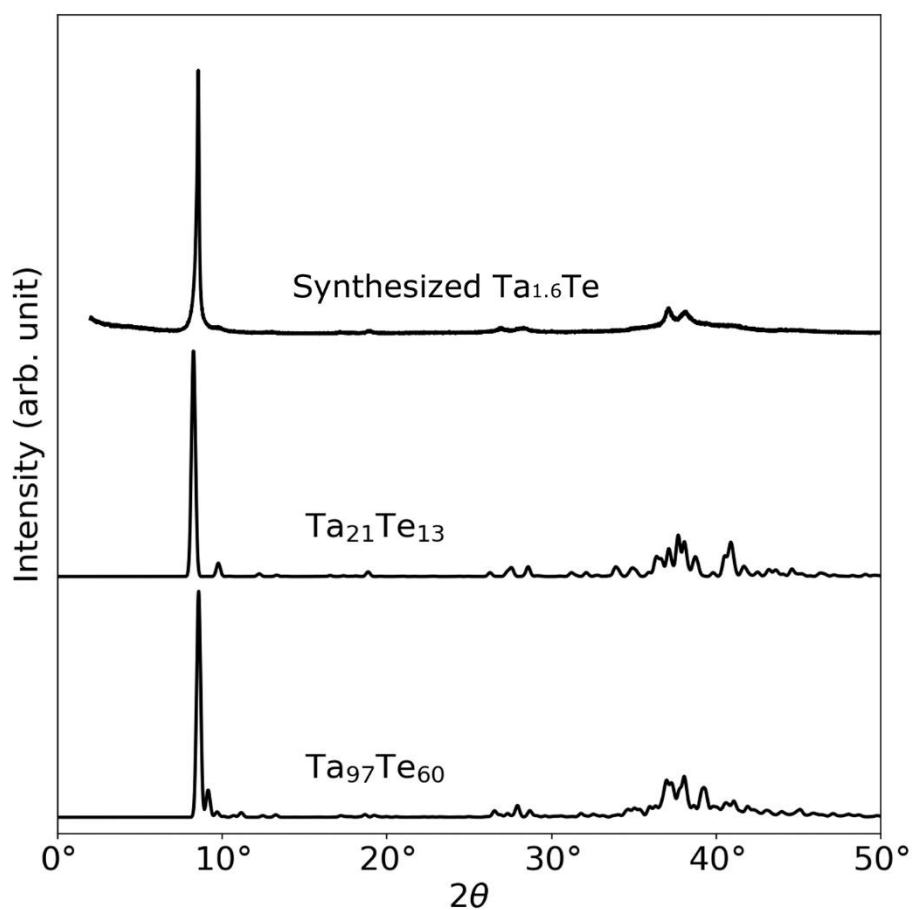
Supplementary Fig. 1 | Powder XRD analysis. Comparison between the experimentally acquired powder XRD profile of the Ta_{1.6}Te sample (Cu K α ₁; $\lambda = 1.5405 \text{ \AA}$) and the peak data of the crystalline phases of TaTe₂ and Ta obtained from 'Powder Diffraction Datafile (PDF)'.



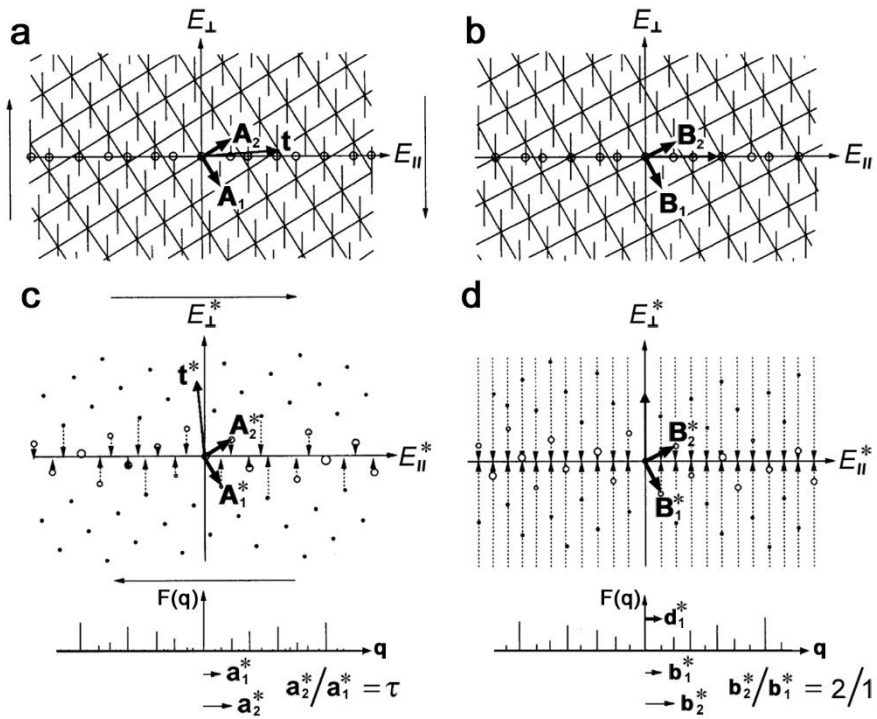
Supplementary Fig. 2 | XRD peak indexing. **a**, A twelve-fold electron diffraction pattern showing the four basis vectors \mathbf{a}_i^* ($i = 1-4$) used for indexing. **b**, Results of the XRD peak indexing.



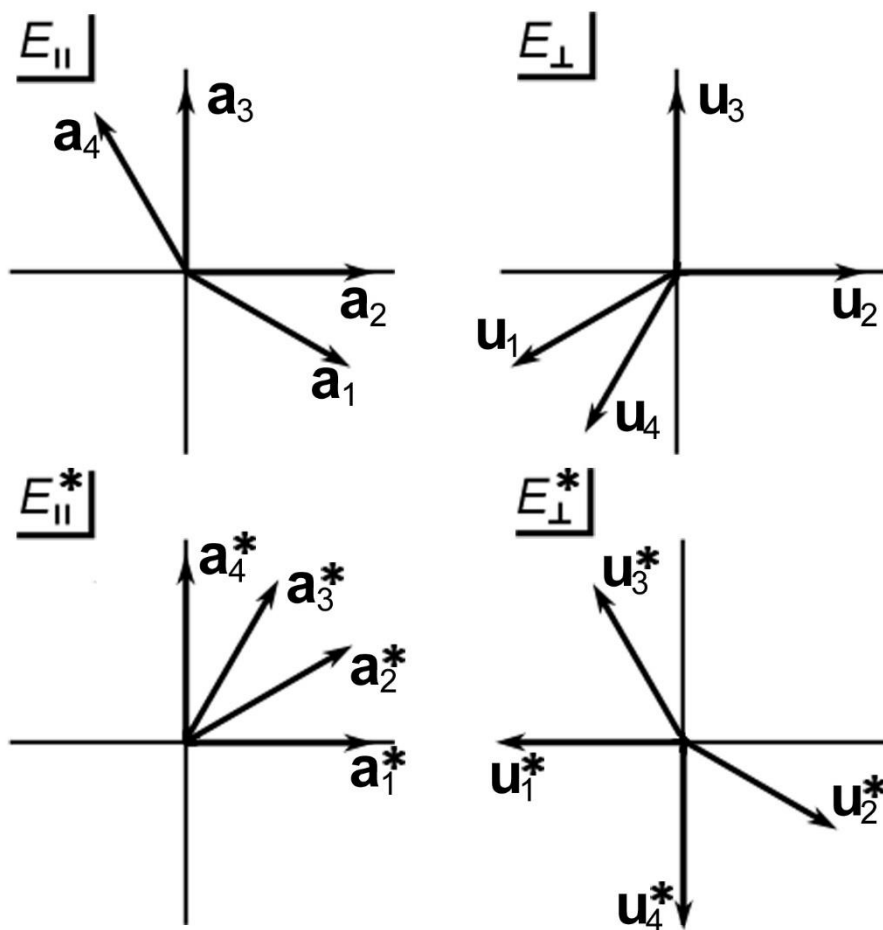
Supplementary Fig. 3 | Structures of the CA phases. a, b, Projections of the $\text{Ta}_{21}\text{Te}_{13}$ (**a**) and $\text{Ta}_{97}\text{Te}_{60}$ (**b**) CA phase structures onto the c -plane^{2,3}. The unit cells of the crystals are indicated in blue, and that of the basic structure in **b** is shown in red.



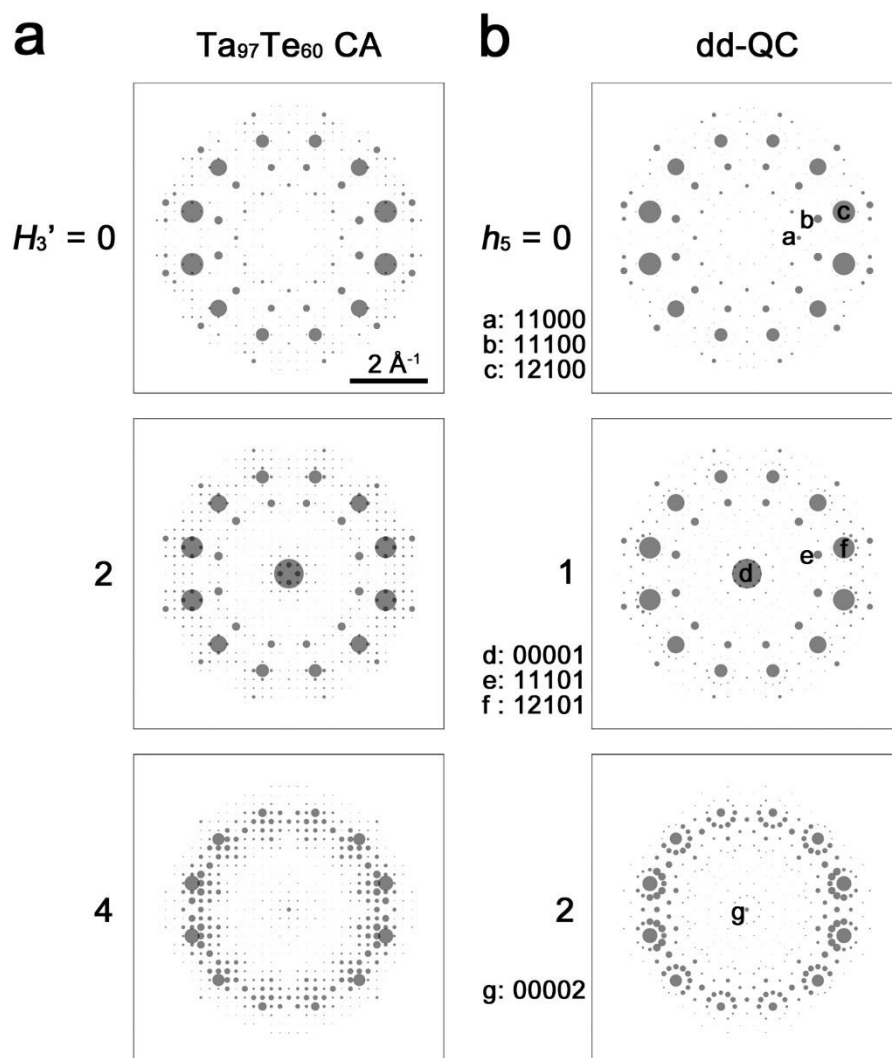
Supplementary Fig. 4 | Powder XRD investigation. Experimentally obtained powder XRD profile of the $Ta_{1.6}Te$ sample ($Cu K\alpha_1$; $\lambda = 1.5405 \text{ \AA}$) and calculated profiles of the $Ta_{21}Te_{13}$ and $Ta_{97}Te_{60}$ CA phases. Gaussians with a full width at half maximum of $\Delta q = 0.02 \text{ \AA}^{-1}$ were used for the calculated profiles.



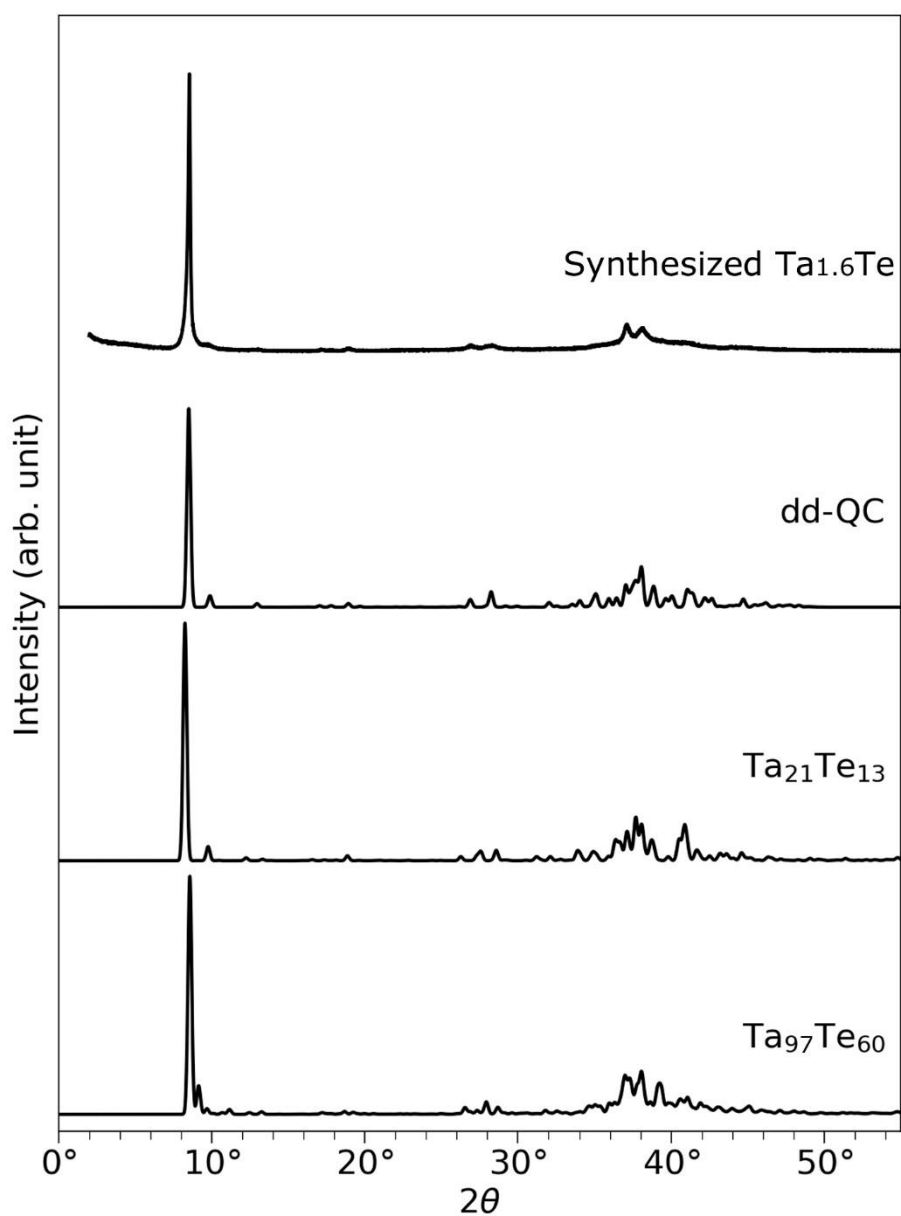
Supplementary Fig. 5 | Relationships between a QC and its CA in real and reciprocal spaces **a**, A 1D quasiperiodic structure, called a Fibonacci lattice, expressed as a 1D section of a 2D periodic structure. **b**, A CA obtained upon imposing a phason strain onto the Fibonacci lattice shown in **(a)**. **c**, **d**, Fourier transforms of the **c**, Fibonacci lattice and **d**, CA.



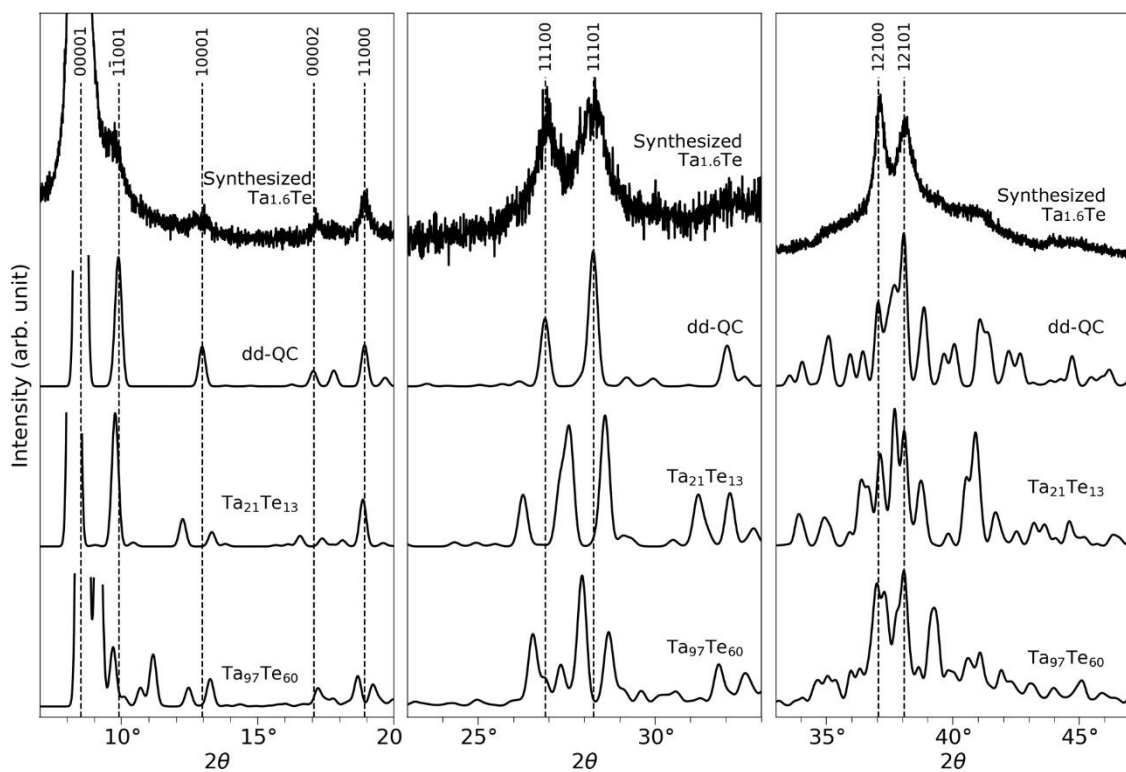
Supplementary Fig. 6 | Projections of the basis vectors of a 4D dodecagonal lattice. Projections of the basis vectors \mathbf{A}_i (\mathbf{A}_i^*) ($i = 1 - 4$) of a 4D dodecagonal lattice (that is, \mathbf{a}_i (\mathbf{a}_i^*) and \mathbf{u}_i (\mathbf{u}_i^*)) onto E_{\parallel} (E_{\parallel}^*) and E_{\perp} (E_{\perp}^*), respectively.



Supplementary Fig. 7 | Diffraction patterns of the CA and dd-QC phases. a, b, Calculated diffraction patterns of the **a**, $\text{Ta}_{97}\text{Te}_{60}$ CA and **b**, dd-QC phases on the planes perpendicular to the c -axis. The area of the circle is proportional to $|F|^2$.



Supplementary Fig. 8 | Powder XRD analysis. Powder XRD profiles acquired for the synthesized Ta_{1.6}Te sample and calculated for the dd-QC, Ta₂₁Te₁₃ CA, and Ta₉₇Te₆₀ CA phases. Gaussians with a full width at half maximum of $\Delta q = 0.02 \text{ \AA}^{-1}$ were used for the calculated profiles.



Supplementary Fig. 9 | Magnified versions of the powder XRD profiles shown in Supplementary Fig. 8. Powder XRD profiles acquired for the synthesized $\text{Ta}_{1.6}\text{Te}$ sample and calculated for the dd-QC, $\text{Ta}_{21}\text{Te}_{13}$ CA, and $\text{Ta}_{97}\text{Te}_{60}$ CA phases. Gaussians with a full width at half maximum of $\Delta q = 0.02 \text{ \AA}^{-1}$ were used for the calculated profiles.